

<https://doi.org/10.1038/s44384-025-00016-7>

A free-field method of characterizing anisotropy in porous media



Mélanie Nolan^{1,2} ✉, Samuel A. Verburg³, Théo Cavalieri¹, Efren Fernandez-Grande² & Jean-Philippe Groby¹

Porous media are commonly described as effective isotropic fluid materials, such that their acoustic properties can be adequately determined from their bulk modulus and dynamic density. Most porous materials, however, possess a marked anisotropy, which influences their acoustical behavior and the parameters necessary to deduce it. Specifically, the influence of anisotropy translates into a full symmetric density tensor, drastically increasing the number of effective fluid parameters required to describe the medium. This paper presents a method for retrieving the bulk modulus and density tensor coefficients of a rigidly-backed layer of anisotropic porous material from reflection coefficients measured in free field with an array of microphones. The procedure consists in estimating the reflection coefficient via sound field reconstruction at the material's surface. The reflection properties are estimated for various angles of incidence, and an inverse problem is formulated to infer the effective fluid parameters. The validity of the method is confirmed numerically on a synthetic porous layer and experimentally on a manufactured glass wool layer. The proposed method enables to characterize anisotropy in porous media non-invasively (solely based on observing the sound field above the material), showing promising potential for the effective characterization of complex media.

Acoustic wave propagation and viscothermal dissipation of acoustic energy in porous media can be described macroscopically by an equivalent fluid model, which requires the knowledge of several pore parameters. Although some of the pore parameters can be measured directly¹, these methods require specialized equipment and are often difficult to carry out. Indirect (inverse) acoustic methods, whereby a measurable acoustical property can be directly related to the pore morphology, are an attractive alternative to direct measurements. Two common acoustical properties that are directly measurable with a standardized impedance tube² are the normal incidence reflection and transmission coefficients, which can be used to predict the behavior of the dynamic density and bulk modulus of the equivalent fluid^{3,4}. If the material is homogeneous and isotropic, these two frequency-dependent fluid parameters are also sufficient to determine the six Johnson-Champoux-Allard-Lafarge (JCAL) parameters^{5,6} that control the dissipation of acoustic energy in the medium⁷.

Most porous media, however, are inherently anisotropic and exhibit different properties along orthogonal directions known as the *principal directions*^{8,9}. In particular, it has been shown that the JCAL parameters that describe visco-inertial dissipation in the medium (high-frequency limit of tortuosity, characteristic viscous length, and static viscous permeability) are

symmetrical tensors of the second order, and diagonal tensors in the orthonormal coordinate system of the medium's principal directions¹⁰⁻¹². This, in turn, is also true for the dynamic density of the equivalent fluid¹², raising to seven (the bulk modulus and the six coefficients of the symmetrical density tensor) the number of effective fluid parameters required to determine (i) the twelve JCAL parameters that account for energy dissipation in anisotropic porous media; (ii) the three angles (or *principal directions*) that describe the orientation of the medium's micro-structure.

Although the acoustical properties of anisotropic media have garnered significant attention over the past several decades^{7-9,13-15}, much of the literature concerned with the experimental characterization of porous materials has neglected their anisotropic behavior, yielding inaccurate pore estimates. A number of studies did extend inversion procedures to characterize anisotropic materials. These studies, however, consider simplistic assumptions on the nature of anisotropy; e.g., anisotropic materials with principal directions belonging to the layer plane interface^{16,17}, or two-dimensional anisotropic materials with principal directions arbitrarily tilted with respect to the reference coordinate system¹⁸⁻²⁰. The only study that characterizes fully anisotropic porous media in three dimensions (i.e., anisotropic porous materials having principal axes tilted in a priori unknown directions) is due to Terroir et al.²¹.

¹Laboratoire d'Acoustique de l'Université du Mans (LAUM), UMR 6613, Institut d'Acoustique - Graduate School (IA-GS), CNRS, Le Mans Université, Le Mans, France. ²Departamento de Ingeniería Audiovisual y Comunicaciones, Universidad Politécnica de Madrid, Madrid, Spain. ³Acoustic Technology, Department of Electrical and Photonics Engineering, Technical University of Denmark, Kgs. Lyngby, Denmark. ✉e-mail: melanie.nolan@upm.es

In a numerical study, they proposed a general method for retrieving the effective fluid parameters of a layer of homogeneous anisotropic material surrounded on both sides by a homogeneous isotropic fluid. The procedure evaluates the reflection and transmission coefficients at six angles of incidence, from which the effective material parameters and the orientation of the material's principal axes are inferred. Experimental validation in an impedance tube was recently achieved by Cavalieri et al.^{22,23}, via measurements of the reflection and transmission coefficients of six samples cut in six different orientations in a layer of glass wool.

In this paper, we propose a free-field experimental procedure to estimate non-invasively the effective fluid parameters, JCAL parameters, and principal directions of a layer of anisotropic porous material. We extend the methodology proposed by Terroir et al.²¹ to rigidly-backed anisotropic porous media, and examine if the effective fluid parameters can be extracted from oblique incidence reflection coefficients measured in free field with an array of microphones (without the use of transmission coefficients). The experimental procedure is based on a recent experimental method developed in refs. 24,25 and consists in estimating the surface impedance via sound field reconstruction (sound pressure and particle velocity) at the material's surface. The reflection properties are estimated for six angles of incidence, and an inverse problem is formulated to infer the effective fluid parameters from the measured reflection coefficients and the sound pressure at the rigid backing. Based on the retrieved fluid parameters, the twelve JCAL parameters and three principal directions are further obtained via optimization.

To date, existing characterization techniques have mostly relied on measurements taken at normal incidence in an impedance tube. The proposed free-field approach transcends classical tube methods in that it enables angle-dependent measurements and opens up the possibility to develop in-situ techniques to characterize materials outside laboratory environments (after installation and in realistic operational conditions). To the authors' knowledge, it is the first time that such methodology is implemented, and it shows promising potential for the effective characterization of complex structures that cannot otherwise be mounted in a tube.

Results

Analytical results

We consider porous materials that are homogeneous (i.e., whose properties are spatially uniform) and whose solid phase is assumed to be motionless. We define a reference coordinate system $(O, \mathbf{e}_1, \mathbf{e}_2, \mathbf{e}_3)$ with position coordinates (x_1, x_2, x_3) . We consider an infinite layer of anisotropic porous material with thickness L , bulk modulus B , and density tensor $\boldsymbol{\rho}$ (see Fig. 1). In the reference coordinate system, its boundaries are defined by the equations $x_3 = 0$ and $x_3 = L$. On the side defined by $x_3 \leq 0$, the layer is fixed on a rigid, impervious wall. On the other side $x_3 \geq L$, the layer is surrounded by an isotropic fluid of scalar density ρ_0 , bulk modulus B_0 , and characteristic impedance $Z_0 = (\rho_0 B_0)^{1/2} = \rho_0 c_0$, where $c_0 = (B_0/\rho_0)^{1/2}$ is the speed of sound. Note that we account for the anisotropy of the layer by using a density tensor, as opposed to a scalar density¹². In particular, the orthonormal coordinate system $(\mathbf{e}_I, \mathbf{e}_{II}, \mathbf{e}_{III})$ of the material's principal directions with position coordinates (x_I, x_{II}, x_{III}) can be defined so that the density tensor is diagonal in this system. That is, the density tensor can be written as $\boldsymbol{\rho} = \boldsymbol{\rho}^* = \text{diag}(\rho_I, \rho_{II}, \rho_{III})$, where ρ_I, ρ_{II} , and ρ_{III} are the principal densities

and the superscript $*$ designates the diagonal tensor. In the reference coordinate system, the density tensor reads $\boldsymbol{\rho} = \mathbf{R}\boldsymbol{\rho}^*\mathbf{R}^T$, where the superscript T denotes non-conjugate transposition and $\mathbf{R} = \mathbf{R}_3(\theta_{III})\mathbf{R}_2(\theta_{II})\mathbf{R}_1(\theta_I)$ is the rotation matrix between the two coordinate systems, with $\mathbf{R}_1, \mathbf{R}_2$, and \mathbf{R}_3 being elementary matrices of rotation and θ_I, θ_{II} , and θ_{III} the roll, pitch, and yaw angles, respectively. In the layer, the pressure and particle velocity fields (p_I, \mathbf{v}_I) are governed by the equations of mass and momentum conservation

$$\begin{cases} i\omega \frac{p_I}{B} = \nabla \cdot \mathbf{v}_I, \\ i\omega \boldsymbol{\rho} \cdot \mathbf{v}_I = \nabla p_I, \end{cases} \quad (1)$$

where $\omega = 2\pi f$ is the angular frequency and time dependency $e^{-i\omega t}$ is omitted.

Let us now consider the incident plane wave $p^i = e^{i(k_1 x_1 + k_2 x_2 - k_3(x_3 - L))}$ propagating in the domain $x_3 \geq L$ with unitary amplitude and the wavenumbers $k_1 = -k_0 \sin \theta \cos \phi$, $k_2 = -k_0 \sin \theta \sin \phi$ and $k_3 = k_0 \cos \theta$, where $k_0 = \omega/c_0$ and θ and ϕ are the elevation and azimuth angles measured from (O, x_3) and (O, x_1) , respectively. The Snell-Descartes law yields the specularly reflected wave $p^r = R e^{ik_3(x_3 - L)} e^{i\mathbf{k}_r \cdot \mathbf{x}_r}$, where R is the pressure reflection coefficient, $\mathbf{k}_r = k_1 \mathbf{e}_1 + k_2 \mathbf{e}_2$, and $\mathbf{x}_r = x_1 \mathbf{e}_1 + x_2 \mathbf{e}_2$. In the layer, the pressure and particle velocity fields p_I and \mathbf{v}_I take the form

$$\begin{cases} p_I = \hat{p}_I(x_3) e^{i\mathbf{k}_r \cdot \mathbf{x}_r}, \\ \mathbf{v}_I = \hat{\mathbf{v}}_I(x_3) e^{i\mathbf{k}_r \cdot \mathbf{x}_r}, \end{cases} \quad (2)$$

where $\hat{p}_I(x_3)$ and $\hat{\mathbf{v}}_I(x_3)$ are independent of \mathbf{x}_r due to the layer being homogeneous, but still depend on the coordinate x_3 . Substituting Eq. (2) into Eq. (1) yields the equations of apparent mass and momentum conservation

$$\begin{cases} i\omega \frac{\tilde{p}_I}{\tilde{B}} = i(\mathbf{q} \cdot \mathbf{k}_r) \tilde{v}_{I3} + \frac{\partial \tilde{v}_{I3}}{\partial x_3}, \\ i\omega \tilde{\rho} \tilde{v}_{I3} = i(\mathbf{q} \cdot \mathbf{k}_r) \tilde{p}_I + \frac{\partial \tilde{p}_I}{\partial x_3}, \end{cases} \quad (3)$$

where $\tilde{v}_{I3} = \hat{\mathbf{v}}_I(x_3) \cdot \mathbf{e}_3$, $\mathbf{q} = q_1 \mathbf{e}_1 + q_2 \mathbf{e}_2$ is a dimensionless vector, and \tilde{B} and $\tilde{\rho}$ are the apparent bulk modulus and density, respectively, where the superscript designates apparent quantities. Denoting the inverse of the density tensor by the symmetric tensor $\mathbf{H} = \boldsymbol{\rho}^{-1}$, the coefficients q_1 and q_2 and the apparent density $\tilde{\rho}$ can be shown to depend on the inverse density tensor components $(h_{11}, h_{12}, h_{13}, h_{22}, h_{23}, h_{33})$ according to²¹

$$q_1 = \frac{h_{13}}{h_{33}}, \quad q_2 = \frac{h_{23}}{h_{33}}, \quad \tilde{\rho} = \frac{1}{h_{33}}. \quad (4)$$

Similarly, the apparent bulk modulus \tilde{B} can be shown to depend on the inverse density tensor, the physical bulk modulus B and the wavenumber vector $\mathbf{k}_r = (k_1, k_2)$ according to²¹

$$\frac{\omega^2}{B} - \frac{\omega^2}{\tilde{B}(k_1, k_2)} = \xi_{11} k_1^2 + \xi_{22} k_2^2 + 2\xi_{12} k_1 k_2, \quad (5)$$

with $\xi_{ij} = h_{ij} - h_{33} q_i q_j, \forall (i, j) \in \{1, 2\}^2$. Details regarding the derivation of Eqs. (3) to (5) can be found in ref. 21. It is worth recalling that the reflection coefficient R , the bulk modulus B , the density tensor $\boldsymbol{\rho}$ and its inverse \mathbf{H} are complex-valued and frequency-dependent variables. The sound pressure and normal component of the particle velocity being continuous at the layer boundaries $x_3 = 0$ (rigid backing) and $x_3 = L$, the boundary conditions read

$$\begin{cases} \hat{p}_I(0) = \hat{p}_0, \\ \hat{v}_{I3}(0) = 0, \\ \hat{p}_I(L) = A(1 + R), \\ \hat{v}_{I3}(L) = A(R - 1)/\tilde{Z}_0, \end{cases} \quad (6)$$

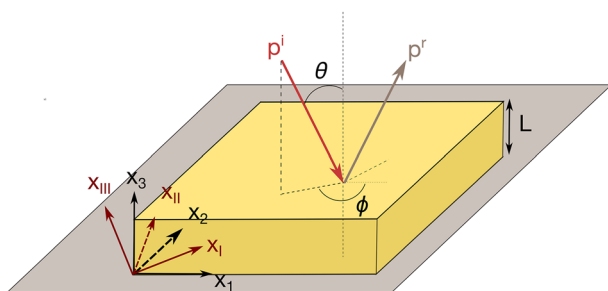


Fig. 1 | Conceptual view. Rigidly-backed homogeneous anisotropic porous layer.

where $A = 1$ corresponds to the unitary amplitude of the incidence wave, \hat{p}_0 is the sound pressure at the rigid backing, and $\tilde{Z}_0 = (\hat{p}_0/\tilde{B}_0)^{1/2} = Z_0/\cos(\theta)$ is the apparent impedance of air in the direction defined by \mathbf{e}_3 . The system of differential equations (3), subject to the boundary conditions described in equation (6), can be written in a matrix form and solved by means of matrix exponential, yielding the system of linear equations:

$$\begin{cases} 2(R+1) = \hat{p}_0(e^{ik_3^-L} + e^{ik_3^+L}) \\ 2(R-1)/\tilde{Z}_0 = (\hat{p}_0/\tilde{Z})(-e^{ik_3^-L} + e^{ik_3^+L}) \end{cases} \quad (7)$$

where $k_3^\pm = -\mathbf{q} \cdot \mathbf{k}_\Gamma \pm \tilde{k}$ and $\tilde{k} = \omega(\tilde{\rho}/\tilde{B})^{1/2}$ and $\tilde{Z} = (\tilde{\rho}\tilde{B})^{1/2}$ are the apparent wavenumber and impedance in the layer, respectively. Solving for \tilde{Z} and \tilde{k} , the apparent impedance reads

$$\tilde{Z} = \pm \tilde{Z}_0 \sqrt{\frac{(R+1)^2 - (\hat{p}_0 e^{-i(\mathbf{q} \cdot \mathbf{k}_\Gamma)L})^2}{(R-1)^2}}, \quad (8)$$

while the apparent wavenumber can be inferred using the single relation

$$e^{\pm i\tilde{k}L} = \left[R \left(1 \pm \frac{\tilde{Z}}{\tilde{Z}_0} \right) + \left(1 \mp \frac{\tilde{Z}}{\tilde{Z}_0} \right) \right] \frac{1}{\hat{p}_0 e^{-i(\mathbf{q} \cdot \mathbf{k}_\Gamma)L}}. \quad (9)$$

Note that the sign in Eq. (8) is determined by the passivity constraint $\text{Re}(\tilde{Z}) \geq 0$. As for Eq. (9), solving for $e^{-i\tilde{k}L}$ will be preferred, since the negative wave carries more energy than the positive x_3 -going wave (the incident wave is defined in the negative x_3 direction). This gives $\tilde{k} = [-\text{ang}(e^{-i\tilde{k}L}) + i\log|e^{-i\tilde{k}L}| + 2n\pi]/L$, where ang is the phase angle and \log is the natural logarithm. The term $2n\pi$ with integer $n \in \mathbb{Z}$ is used to unwrap the phase of $e^{-i\tilde{k}L}$, ensuring that \tilde{k} is continuous over all frequencies. The value of the integer n has to be determined and will depend on the nature of the material (typically, $n = 0$ when initiating the procedure at very low frequencies). Equations (8) and (9), which correspond to the Nicolson-Ross-Weir procedure^{26,27} extended to oblique incidence in anisotropic media, show that the apparent impedance and wavenumber (and subsequently the apparent density and bulk modulus) can be retrieved from knowledge of the layer's thickness L , the sound pressure at the rigid backing \hat{p}_0 , and the reflection coefficient R and phase delay $(\mathbf{q} \cdot \mathbf{k}_\Gamma)L$ at specific angles of incidence specified by the wavenumber vector $\mathbf{k}_\Gamma = (k_1, k_2)$. The inverse problem used to retrieve the value of the physical bulk modulus B and the six components of the symmetric inverse density tensor ($h_{11}, h_{12}, h_{13}, h_{22}, h_{23}, h_{33}$) is formulated in the Methods section. The oblique-incidence reflection coefficient is estimated from the plane wave model

$$R = \frac{Z_s \cos(\theta) - 1}{Z_s \cos(\theta) + 1}, \quad (10)$$

where Z_s is the material's normalized surface impedance. The surface impedance is measured in free field via reconstruction of the sound pressure and particle velocity at the material's surface. This is also detailed in the Methods section.

Numerical results

The validity of the method is first examined numerically by means of simulated measurements in MATLAB. To this end, we consider an anisotropic homogeneous layer of thickness $L = 3$ cm and infinite extent, with known porous properties. In its thickness, the layer is formed by the repetition of unit cells consisting of an orthorhombic lattice with dimensions $\ell_I = \ell_c$, $\ell_{II} = 2\ell_c$ and $\ell_{III} = 3\ell_c$, from which an ellipsoid with semi-axes $r_I = 0.66\ell_c$, $r_{II} = 1.32\ell_c$, and $r_{III} = 1.98\ell_c$ is carved out, where $\ell_c = 200 \mu\text{m}$ is the characteristic pore size. Note that we use the same material as in ref. 21. The choice of the characteristic pore size guarantees

that the condition of scale separation is satisfied in the frequency range of interest¹⁰. Besides, the layer includes 150 unit cells in its thickness, guaranteeing a bulk behavior of the material.

The anisotropic layer is described in the orthonormal coordinate system $(\mathbf{e}_I, \mathbf{e}_{II}, \mathbf{e}_{III})$ of its principal directions with a diagonal density tensor $\boldsymbol{\rho}^*$. Each principal density ρ_J (with $J = \text{I, II, III}$) of the diagonal density tensor, as well as the bulk modulus B are approximated using the JCAL model for anisotropic rigid-framed porous media⁶

$$\begin{cases} \rho_J = \frac{\alpha_J^\infty \rho_0}{\phi} \left(1 - \frac{\eta \phi}{i\omega \rho_0 k_{0,J} \alpha_J^\infty} \sqrt{1 - \frac{i4(\alpha_J^\infty)^2 k_{0,J}^2 \rho_0 \omega}{\eta \Lambda_J^2 \phi^2}} \right), \\ B = \frac{\frac{\gamma P_0}{\phi}}{\gamma - (\gamma - 1) \left(1 + \frac{i\phi \kappa}{k_0^2 C_p \rho_0 \omega} \sqrt{1 - \frac{i4k_0^2 C_p \rho_0 \omega}{\kappa \Lambda^2 \phi^2}} \right)^{-1}}, \end{cases} \quad (11)$$

where the air properties (density ρ_0 , dynamic viscosity η , specific heat ratio γ , thermal conductivity κ , and specific heat at constant pressure C_p) can be calculated from the temperature $T = 20$ °C and the atmospheric pressure $P_0 = 101320$ Pa²⁸. In this case, the JCAL model relies on homogenized properties of the unit cell, which are calculated using the two-scale asymptotic homogenization method²⁹. This results in the twelve pore parameters listed in Table 1, where the pore parameters describing the thermo-acoustic dissipation (open porosity ϕ , thermal characteristic length Λ' and static thermal permeability k_0') are scalar quantities, while the pore parameters describing the visco-inertial dissipation (high-frequency limit of the tortuosity α_J^∞ , viscous characteristic length Λ_J and static viscous permeability $k_{0,J}$) are direction-dependent quantities. Finally, the diagonal density tensor $\boldsymbol{\rho}^*$ is rotated by the roll, pitch, and yaw angles $\theta_I = 30^\circ$, $\theta_{II} = 45^\circ$ and $\theta_{III} = 60^\circ$ to result in a fully-anisotropic density tensor $\boldsymbol{\rho}$, and its inverse \mathbf{H} .

The array used for the simulated measurement consists of 162 microphones, arranged in two square layers of 9×9 microphones each, with a vertical spacing of 3 cm between the two layers, a horizontal spacing of 2.5 cm, and an array aperture of 20 cm \times 20 cm. Considering the minimum

Table 1 | Homogenized JCAL parameters for an anisotropic unit cell with characteristic pore size $\ell_c = 200 \mu\text{m}$

	ϕ (1)	Λ' (μm)	k_0' (nm^2)	α_J^∞ (1)	Λ_J (μm)	$k_{0,J}$ (nm^2)
Ω	0.91	368	8	–	–	–
\mathbf{e}_I	–	–	–	1.18	204	4.4
\mathbf{e}_{II}	–	–	–	1.06	240	3.2
\mathbf{e}_{III}	–	–	–	1.04	269	3.6

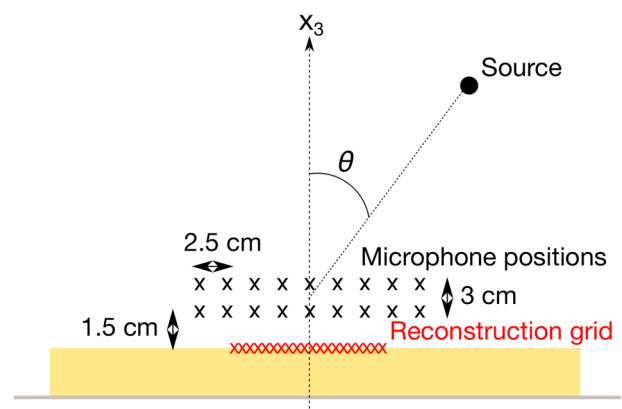
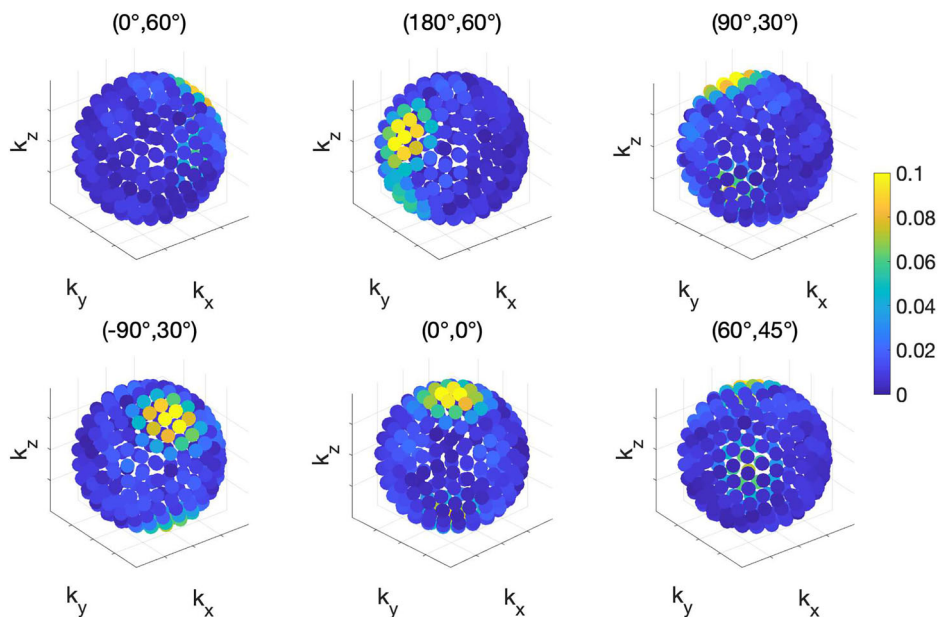


Fig. 2 | Sketch of the measurement principle (2D view). The porous layer is shown in yellow. The black markers correspond to the microphone positions, while the red markers denote the reconstruction grid.

Fig. 3 | Wavenumber representation. Magnitude (Pa) of the wavenumber spectrum coefficients estimated at 1 kHz for the six angles of incidence $(\phi, \theta) = (0, 60^\circ), (180^\circ, 60^\circ), (90^\circ, 30^\circ), (-90^\circ, 30^\circ), (0^\circ, 0^\circ),$ and $(60^\circ, 45^\circ)$.



and maximum distances between transducers, the effective frequency range of the array is approximately 200 Hz to 5 kHz. The array is placed at a distance of 1.5 cm from the material surface (see Fig. 2).

The pressure measured at the 162 microphone positions is modeled as the sum of an incident plane wave p^i , and a specularly reflected plane wave p^r , where the reflection coefficient R is calculated from

$$R = \frac{\cos(\tilde{k}L) + i(\tilde{Z}_0/\tilde{Z})\sin(\tilde{k}L)}{\cos(\tilde{k}L) - i(\tilde{Z}_0/\tilde{Z})\sin(\tilde{k}L)}, \quad (12)$$

and the pore parameters defined in Table 1. The sound pressure \hat{p}_0 at the rigid backing is simulated based on

$$\hat{p}_0 = \frac{2e^{i(\mathbf{q}\cdot\mathbf{k}_r)L}}{\cos(\tilde{k}L) - i(\tilde{Z}_0/\tilde{Z})\sin(\tilde{k}L)}. \quad (13)$$

Gaussian noise with signal-to-noise ratio (SNR) of 40 dB is added to both simulated pressures (note that Eqs. (12) and (13) follow from solving the system of linear equations (7) for R and \hat{p}_0). Six different angles of incidence are considered: $(\phi, \theta) = (0, 60^\circ), (180^\circ, 60^\circ), (90^\circ, 30^\circ), (-90^\circ, 30^\circ), (0^\circ, 0^\circ),$ and $(60^\circ, 45^\circ)$, which will be used for retrieving the effective fluid parameters. Additional angles of incidence could be used to obtain an overdetermined problem and improve the estimation, if needed.

The pressure measured at the 162 microphone positions is further expanded into a plane-wave basis of 256 plane waves, whose directions of propagation are uniformly distributed over a spherical domain. This plane-wave basis is used to extrapolate the sound pressure and normal component of the particle velocity at the sample’s surface, at 20×20 points on a square grid of dimensions $10 \text{ cm} \times 10 \text{ cm}$. Based on the reconstructed sound pressure and particle velocity, a normalized surface impedance is calculated at each point of the grid, although the material’s surface impedance is eventually estimated as the spatial average over the grid. Note, however, that the size of the reconstruction grid ensures small spatial deviations of the surface impedance in the frequency range of interest. Finally, the estimated reflection coefficient is calculated from the plane wave model defined in Eq. (10) for each angle of incidence.

Figure 3 shows the magnitude of the plane wave expansion at 1 kHz for the six angles of incidence $(\phi, \theta) = (0, 60^\circ), (180^\circ, 60^\circ), (90^\circ, 30^\circ), (-90^\circ, 30^\circ), (0^\circ, 0^\circ)$ and $(60^\circ, 45^\circ)$, respectively. The magnitude of the 256 plane waves is represented in Pascals. For each angle of incidence, the directions of arrival of the incident and reflected waves are clearly identified, with the maximum

amplitudes corresponding to the incident directions. Figure 4 shows the corresponding reflection coefficients as a function of frequency. The estimated coefficients show excellent agreement with those obtained from solving Eq. (12) directly.

Once the reflection coefficients have been estimated, the retrieval procedure described in the Methods section is applied to infer the bulk modulus B and the six components of the inverse density tensor $(h_{11}, h_{12}, h_{13}, h_{22}, h_{23}, h_{33})$. The estimated parameters are displayed in Fig. 5 as a function of frequency. The estimated coefficients agree well with those obtained from solving the direct problem directly (i.e., based on the pore parameters defined in Table 1). It is interesting to note that some of the parameters are better estimated than others. The procedure yields a particularly accurate estimate for the component h_{33} , which results from averaging six independent estimates over the six angles of incidence. In contrast, slight discrepancies are observed for the component h_{12} . This is due to the fact that h_{12} exhibits rather small values that depend on the prior (correct) estimation of h_{33}, h_{13}, h_{23} , and B . Nonetheless, the overall numerical results indicate that the proposed method can successfully estimate the density matrix and bulk modulus of a layer of rigidly-backed anisotropic porous material.

Experimental results

In this section, the validity of the method is examined experimentally via free-field measurements on a commercial glass wool sample of thickness 100 mm (Industry Modus 100 mm, Saint-Gobain Ecophon, Hyllinge, Sweden). The measurements are performed in a large anechoic chamber at the Technical University of Denmark (Kgs. Lyngby, Denmark), as shown in Fig. 6.

Reflection coefficients are measured for the six angles of incidence $(\phi, \theta) = (0, 60^\circ), (180^\circ, 60^\circ), (90^\circ, 30^\circ), (-90^\circ, 30^\circ), (0^\circ, 0^\circ)$ and $(60^\circ, 45^\circ)$ using the same array geometry, plane-wave basis and reconstruction grid as in the numerical study. The retrieval procedure is then used to calculate the corresponding bulk modulus B and individual components of the inverse density tensor \mathbf{H} . Finally, based on these measured fluid parameters, the complete set of anisotropic JCAL parameters as well as the orientation of the material’s principal axes are reconstructed via Particle Swarm Optimization, as described in ref. 23. These parameters and angles are further used to infer reconstructed values of R, B , and \mathbf{H} and validate the reflection coefficients and effective fluid parameters measured in free field. The routines for the optimization are implemented within MATLAB using the function `particleswarm` from the *Global Optimization Toolbox*. The JCAL parameters and principal directions are recovered based on the minimization of

Fig. 4 | Reflection coefficients (simulated). Estimated (dotted line) and theoretical (solid line) reflection coefficient of a layer of anisotropic fluid material made of an orthorhombic lattice of overlapping ellipsoids. Six angles of incidence are considered: $(\phi, \theta) = (0, 60^\circ)$, $(180^\circ, 60^\circ)$, $(90^\circ, 30^\circ)$, $(-90^\circ, 30^\circ)$, $(0^\circ, 0^\circ)$, and $(60^\circ, 45^\circ)$.

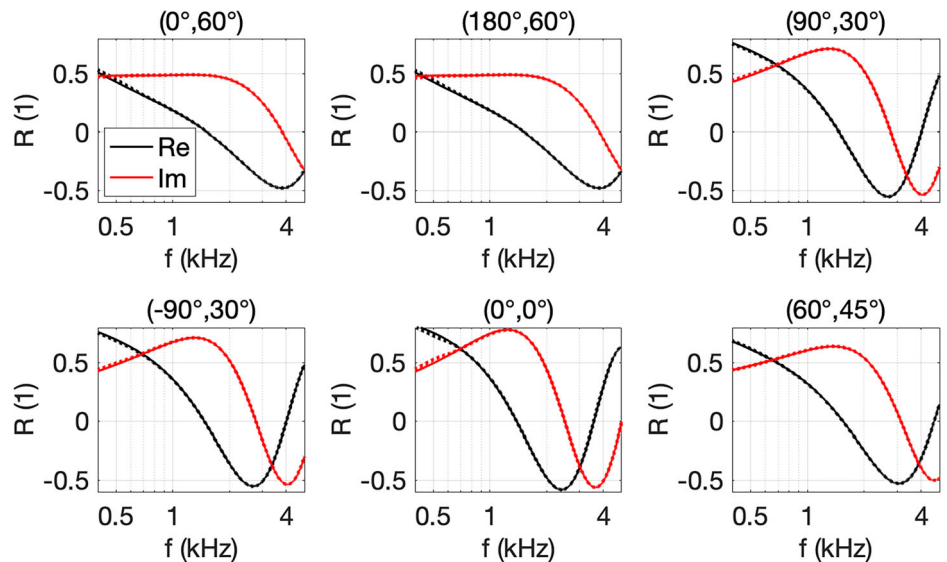
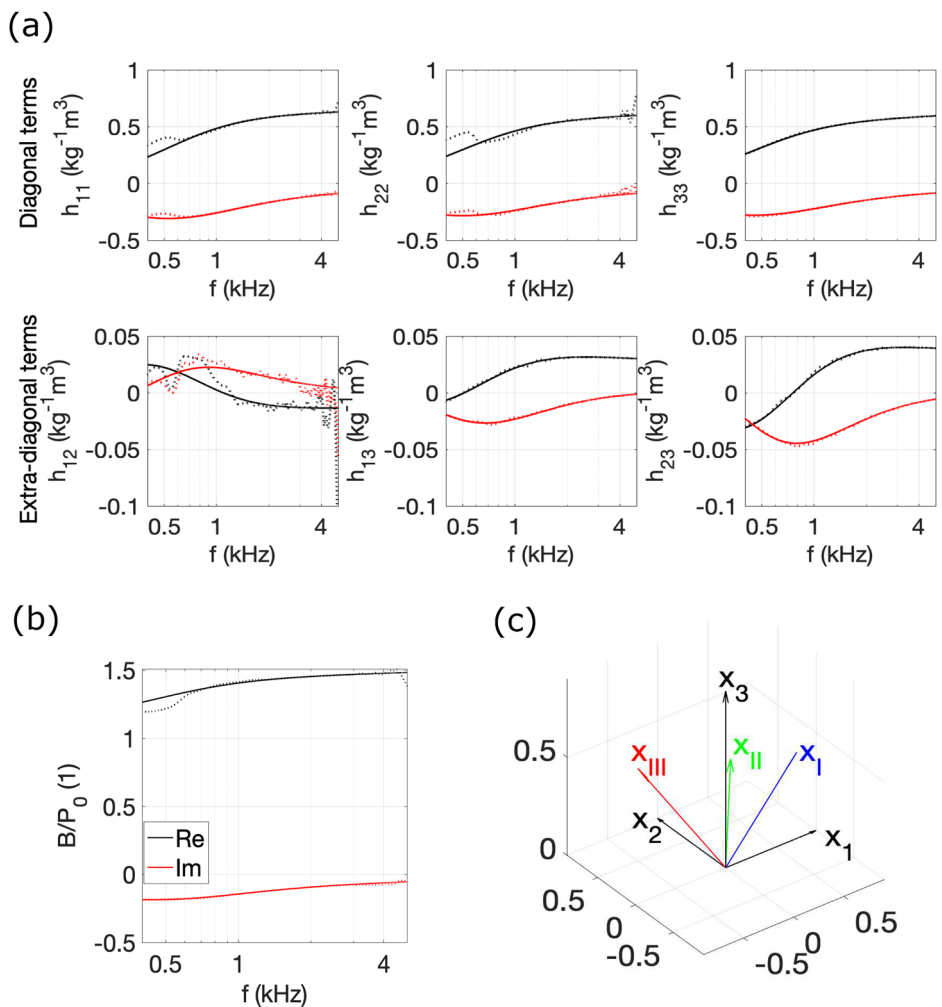


Fig. 5 | Equivalent fluid properties (simulated). **a** Estimated (dotted line) and theoretical (solid line) inverse density tensor coefficients of a layer of rigidly-backed anisotropic fluid material made of an orthorhombic lattice of overlapping ellipsoids. Black: real part. Red: imaginary part. **b** Estimated (dotted line) and theoretical (solid line) normalized bulk modulus. Black: real part. Red: imaginary part. **c** Orientation of the principal directions.



two cost functions: first, the 3 thermo-acoustic parameters (ϕ , Λ' and k'_0) are obtained by minimizing the error between the measured and reconstructed bulk modulus; further, the 9 visco-inertial parameters (α_J^∞ , Λ_J , and $k_{0,J}$, with $J = \text{I, II, III}$) and 3 principal directions θ_I , θ_{II} , and θ_{III} are retrieved by minimizing the error between the measured and reconstructed coefficients

of the inverse density tensor. For details regarding the optimization procedure as well as a discussion on the convergence of the estimated parameters, the interested reader is referred to²³.

The reconstructed JCAL parameters and principal directions obtained via optimization are summarized in Table 2. An angle of 47° is found along

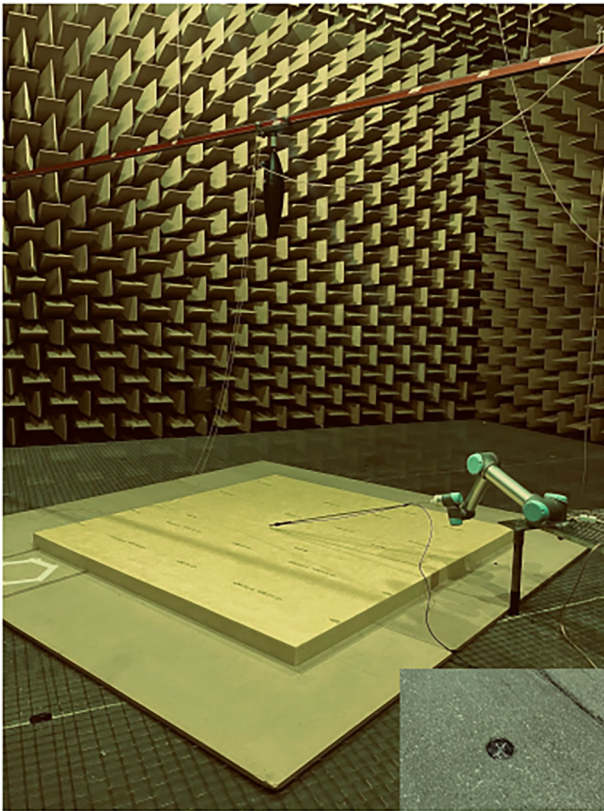


Fig. 6 | Measurement setup in the anechoic chamber. An additional microphone is flush-mounted at the interface between the porous layer and the rigid backing.

Table 2 | Reconstructed values of the JCAL parameters and principal directions for the glass wool

	ϕ (1)	Λ' (μm)	k'_0 (nm^2)	$\alpha_{33}^>$ (1)	Λ_j (μm)	$k_{0,j}$ (nm^2)	θ ($^\circ$)
Ω	0.95 (0.99)	300 (184)	2.9 (3.1)	–	–	–	–
\mathbf{e}_I	–	–	–	1.2	55	0.77	0
\mathbf{e}_{II}	–	–	–	1.2	231	2.3	0
\mathbf{e}_{III}	–	–	–	1 (1.01)	73 (82)	1.3 (1.46)	47

In parentheses: Comparison with direct measurements in the normal direction³⁰.

the normal direction, indicating that the glass wool fibers are rotated in the absorber plane. The JCAL parameters are compared with parameters directly measured via standardized measurements in the normal direction (in parentheses). These measurements were performed by Matelys, Vaulx-en-Velin, France³⁰. There is very good agreement between the reconstructed JCAL parameters and the direct measurements. A slight discrepancy is observed for the thermal characteristic length Λ' , which is however not a defining parameter for such glass wool, making it harder to detect³⁰. It is expected that using a simpler model with fewer pore parameters may be better suited to this specific glass wool and prevent overfitting. Also note that the presence of noise in the input data (B and H) can hinder the performance of the optimization procedure, leading to less accurate predictions. Accuracy can however be improved by measuring additional angles of incidence, allowing to average and stabilize the values of B and H (as seen with the recovery of h_{33} in the Numerical Results section [in Fig. 5]).

In light of the obtained parameters (and, specifically, of the static viscous permeability values), it should be remarked that, strictly speaking, the frame may not be considered rigid in the entire frequency range of interest. The frequency criterion proposed by Biot³¹ can be used, which gives a high critical frequency limit below which the frame may be excited by the motion of air. This frequency is expressed as the ratio of the airflow resistivity $\sigma_1 = \eta/k_{0,j}$ of the porous material, over the density of the interstitial fluid ρ_0 : $f_{\text{Biot}} = \sigma_1/(2\pi\rho_0)$. Applied to the glass-wool sample in the normal direction (i.e., using the flow resistivity value directly measured by Matelys), the criterion would not allow the use of the JCAL model below 1680 Hz. Nevertheless, in this study, and as it is often done in the literature to reduce the number of degrees of freedom in the poroelastic modeling, the equivalent fluid approximation will be used in the entire frequency range of interest: 400 Hz–5 kHz. Strictly, one could consider using a poroelastic Biot model or a limp model to characterize the glass-wool sample in the low-frequency range. This would however be at the expense of modeling and experimentation complexity, and could potentially affect the parameter estimation (influencing the conditioning or inversion properties of the problem). This is, however, out of the scope of the present study.

Figure 7 shows the reflection coefficient measured in free field for the six angles of incidence $(\phi, \theta) = (0, 60^\circ), (180^\circ, 60^\circ), (90^\circ, 30^\circ), (-90^\circ, 30^\circ), (0^\circ, 0^\circ)$ and $(60^\circ, 45^\circ)$ as a function of frequency. There is generally good agreement between the measured and reconstructed reflection coefficients; i.e., the coefficients directly derived from the JCAL parameters and angles obtained via optimization. It is interesting to note that this is also the case below the critical Biot frequency, which warrants the use of the equivalent fluid approximation in the entire frequency range (the frame may not be

Fig. 7 | Reflection coefficients (experimental). Measured (dotted line) and reconstructed (solid line) reflection coefficients for the glass wool. Six angles of incidence are considered: $(\phi, \theta) = (0, 60^\circ), (180^\circ, 60^\circ), (90^\circ, 30^\circ), (-90^\circ, 30^\circ), (0^\circ, 0^\circ)$, and $(60^\circ, 45^\circ)$.

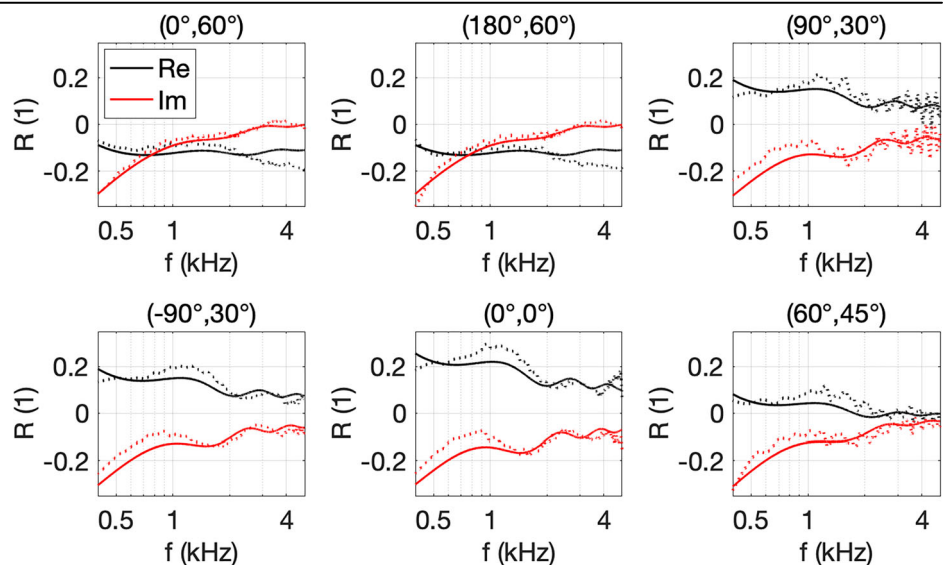
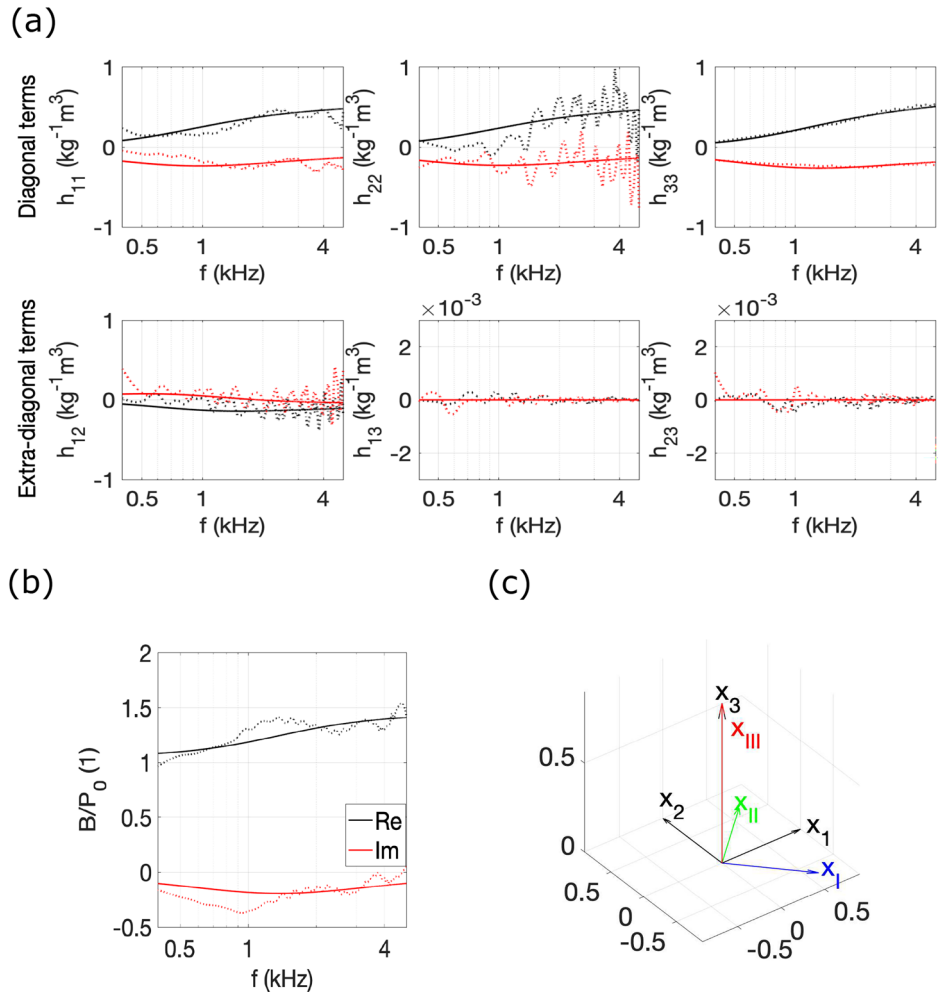


Fig. 8 | Equivalent fluid properties (experimental). **a** Measured (dotted line) and reconstructed (solid line) inverse density tensor coefficients of a layer of rigidly-backed glass wool. Black: real part. Red: imaginary part. **b** Measured (dotted line) and reconstructed (solid line) normalized bulk modulus. Black: real part. Red: imaginary part. **c** Orientation of the principal directions.



much affected by the motion of air in the frequency range 400 Hz–1680 Hz). The measured reflection coefficients show larger deviations for $\theta = 60^\circ$, because the normal component of the particle velocity is smaller towards grazing incidence and therefore more sensitive to noise²⁴. For a discussion on reconstruction errors, the interested reader is referred to refs. 32,33 and²⁴.

Figure 8 shows the measured bulk modulus and individual coefficients of the inverse density tensor as a function of frequency. The measured effective fluid parameters compare well with those obtained from the optimized JCAL parameters and principal directions. Similar to the numerical results, h_{33} compares particularly well, as it is estimated independently and averaged over the six angles of incidence considered in the retrieval procedure. On the contrary, h_{12} is rather poorly estimated, due to the fact that it exhibits small values that depend on the prior (correct) estimation of h_{33} , h_{13} , h_{23} , and B , and is therefore more sensitive to error propagation. Yet, the method has been presented on the basis of only six angles of incidence (which is the minimum required). It is also interesting to note that one of the extra-diagonal terms, h_{12} , is not negligible, indicating that the glass wool sample is not transversely isotropic (as would typically be expected for this type of glass wool). This suggests that the sample presents some additional degree of anisotropy. Specifically, the glass wool fibers appear to be rotated by an angle of 47° in the absorber plane (see Table 2), seemingly due to the manufacturing process. Ultimately, the results presented in the current study show that, based on relatively simple measurements of the sound pressure at the material’s surface, the proposed free-field method enables not only to retrieve the complete set of effective fluid parameters and anisotropic JCAL parameters, but also provides insight into the material’s micro-structure.

Finally, it is interesting to note that the results presented in the current study are in line with the experimental observations presented by Cavalieri et al.²³, who estimated the inverse density tensor coefficients of the same glass wool from reflection and transmission coefficients measured on six samples placed with six different orientations in an impedance tube. As it is not possible to compare the reconstructed JCAL parameters with direct measurements in the tangential directions, the results independently obtained for the material mounted in the tube and for the material mounted in free field can be benchmarked against each other. It can be seen that the reconstructed JCAL parameters for the material mounted in the tube and for the material mounted in free field exhibit similar values (note that the axes x_1 and x_3 have been swapped in ref. 23), indicating that both methods yield reasonable estimates. We do not expect the reconstructed h_{ij} coefficients and JCAL parameters to be identical for the material mounted in the tube and the material mounted in free field due to the presence of local heterogeneity in the tube samples. We hypothesize that averaging over a larger number of tube samples would smooth out the local heterogeneity, leading to porous parameters that are closer to those measured in free field on a larger sample.

Discussion

A free-field method of characterizing the effective fluid properties of rigidly-backed anisotropic porous media with unknown principal directions has been proposed. The method relies on the measurement of the reflection coefficient at a few incidence angles, via sound field reconstruction with an array of microphones. The method was successfully applied to retrieve the bulk modulus and all six components of the symmetric density tensor of a

layer of glass wool with unknown porous properties. Based on the retrieved effective fluid parameters, the full set of anisotropic JCAL parameters, as well as the glass wool's principal directions, could also be recovered via optimization.

The proposed method is the first acoustical holography framework enabling to characterize the micro-structure of anisotropic porous media from fairly simple measurements of the sound pressure in free field. This is unprecedented and paves the way for the experimental characterization of metamaterials and other complex structures that cannot be suitably mounted in a tube or otherwise characterized via established measurement techniques.

Methods

Inverse problem formulation (retrieval procedure)

The coefficients q_1 and q_2 are retrieved from $e^{2iq_1k_1L} = \frac{\hat{p}_0(k'_1,0)}{p_0(-k'_1,0)}$ and $e^{2iq_2k_2L} = \frac{\hat{p}_0(0,k'_2)}{p_0(0,-k'_2)}$ [Eq. (13)] using two pairs of incident waves $(k'_1, 0)$, $(-k'_1, 0)$ and $(0, k'_2)$, $(0, -k'_2)$. This result shows that the apparent impedance and wavenumber (and consequently the apparent density and bulk modulus) are not only known for $\mathbf{k}_T = \pm k'_1 \mathbf{e}_1$ and $\mathbf{k}_T = \pm k'_2 \mathbf{e}_2$, but they can now be assessed for any incident wave. In particular, the physical bulk modulus B is retrieved from Eq. (5) at normal incidence $(k_1, k_2) = (0, 0)$ and reads $B = \tilde{B}(0, 0)$. Further, the coefficients ξ_{11} and ξ_{22} are retrieved from $\xi_{11} = \frac{\omega^2}{k_1^2} \left(\frac{1}{B} - \frac{1}{\tilde{B}(k'_1, 0)} \right)$ and $\xi_{22} = \frac{\omega^2}{k_2^2} \left(\frac{1}{B} - \frac{1}{\tilde{B}(0, k'_2)} \right)$ [Eq. (5)] using the two incident waves $(k'_1, 0)$ and $(0, k'_2)$. Finally, the coefficient ξ_{12} is found from Eq. (5) using a sixth incident wave (k''_1, k''_2) and reads $\xi_{12} = \frac{\omega^2}{2k''_1 k''_2} \left(\frac{1}{B} - \frac{1}{\tilde{B}(k''_1, k''_2)} \right) - \frac{\xi_{11} k''_1}{2k''_1} - \frac{\xi_{22} k''_2}{k''_1}$. The coefficients h_{13} , h_{23} , and h_{33} , are then retrieved from Eq. (4), and the coefficients h_{12} , h_{11} , and h_{22} are given by $h_{12} = \xi_{12} - h_{33} q_1 q_2$, $h_{11} = \xi_{11} - h_{33} q_1^2$, and $h_{22} = \xi_{22} - h_{33} q_2^2$, respectively. For a discussion on the sensitivity of the inverted parameters to variations in the reflection coefficients, the interested reader is referred to the Supplementary Information (Supplementary Figs. 1 and 2).

Oblique-incidence reflection coefficients estimation

The measured pressures $p(\mathbf{r}_m)$ at the M microphone positions \mathbf{r}_m are represented locally as the superposition of N propagating plane waves, with directions of propagation uniformly distributed over a spherical domain³⁴ $p(\mathbf{r}_m) = \sum_{n=1}^N P(\mathbf{k}_n) e^{i\mathbf{k}_n \cdot \mathbf{r}_m}$, where the amplitude term $P(\mathbf{k}_n)$ is the so-called wavenumber (or angular) spectrum³⁵. Each plane wave travels in a direction specified by the wave vector $\mathbf{k}_n = (k_{n1}, k_{n2}, k_{n3}) \in \mathbb{R}^3$ with $k_n^2 = k_{n1}^2 + k_{n2}^2 + k_{n3}^2$, indicating that evanescent waves are not included. As detailed in the Experimental setup description, this is achieved by ensuring that the measurement aperture is placed sufficiently far away from the source and sample edges. The problem can be expressed with the linear model

$$\mathbf{p} = \mathbf{S}\mathbf{a}, \tag{14}$$

where $\mathbf{p} \in \mathbb{C}^M$ contains the measured pressures, $\mathbf{a} \in \mathbb{C}^N$ contains the unknown plane-wave amplitudes, and $\mathbf{S} \in \mathbb{C}^{M \times N}$ is a sensing matrix containing the plane-wave functions $S_{mm} = e^{i\mathbf{k}_n \cdot \mathbf{r}_m}$. As there are more unknown coefficients than measurement points (a large number of elementary plane waves is used to ensure a sufficient spatial resolution of the sound field), the problem is underdetermined (rank-deficient) and requires regularization. The solution $\hat{\mathbf{a}}$ of Eq. (14) is calculated in a least-squares sense, i.e., via regularized matrix pseudo-inverse³⁶. The problem is formulated as an unconstrained optimization problem, introducing a regularization parameter λ that determines the penalty weight of the ℓ_2 -norm of the solution vector $\hat{\mathbf{a}} = \arg \min(\|\mathbf{S}\mathbf{a} - \mathbf{p}\|_2^2 + \lambda \|\mathbf{a}\|_2^2)$, which has the closed-form analytical solution³⁶

$$\hat{\mathbf{a}} = \mathbf{S}^\dagger (\mathbf{S}\mathbf{S}^\dagger + \lambda \mathbf{I})^{-1} \mathbf{p}, \tag{15}$$

where the superscript \dagger denotes conjugate transposition and \mathbf{I} is the identity matrix. Equation (15) corresponds to the least-squares solution of the problem with Tikhonov regularization³⁷. In this study, the L-curve criterion³⁸ is used as a (regularization) parameter-choice method. Once the coefficients $\hat{\mathbf{a}}$ have been determined, the sound pressure and normal component of the particle velocity are reconstructed at a set of G positions \mathbf{r}_g of the material's surface

$$\begin{cases} \hat{\mathbf{p}} = \mathbf{S}_g \hat{\mathbf{a}}, \\ \hat{\mathbf{u}}_{x_3} = \frac{1}{i\omega\rho_0} \frac{\partial \hat{\mathbf{p}}}{\partial x_3} \hat{\mathbf{a}}, \end{cases} \tag{16}$$

where $\hat{\mathbf{p}} \in \mathbb{C}^G$ contains the reconstructed sound pressures, $\hat{\mathbf{u}}_{x_3} \in \mathbb{C}^G$ is the reconstructed normal particle velocity vector, $\mathbf{S}_g \in \mathbb{C}^{G \times N}$ is a reconstruction matrix containing the plane wave functions evaluated at the reconstruction points \mathbf{r}_g , and $\frac{\partial \hat{\mathbf{p}}}{\partial x_3} \in \mathbb{C}^{G \times N}$ contains the partial derivative of the reconstruction matrix in the normal direction. Next, the point-wise normalized surface impedance at position \mathbf{r}_g is calculated with

$$Z_s(\mathbf{r}_g) = \frac{-1}{\rho_0 c_0} \frac{\hat{p}(\mathbf{r}_g)}{\hat{u}_{x_3}(\mathbf{r}_g)}. \tag{17}$$

As the material is assumed homogeneous, the estimated surface impedance is averaged over the G reconstruction points $\tilde{Z}_s = \frac{1}{G} \sum_{g=1}^G Z_s(\mathbf{r}_g)$ to smooth out random errors due to noise²⁴. Finally, the reflection coefficient is calculated from the plane wave model in Eq. (10), using the estimated surface impedance \tilde{Z}_s . Note that Eq. (10) was derived under the assumption of plane wave incidence on an infinite sample¹¹. Yet, as the material is considered to be large enough for the acoustic field at the edges to be negligible in the frequency range of interest, Eq. (10) can be used as an approximation (previous studies dealing with samples and backing plates of similar sizes^{24,25} indicate that edge effects from the sample and backing plate edges were only visible below 400 Hz).

Experimental setup description

The anechoic chamber used for the measurements has an approximate volume of 1000 m³, ensuring free-field conditions down to 100 Hz. A glass wool sample of dimensions 2.4 × 2.4 m is placed on a backing plate of approximately 14 m², and a 1/2 inch pressure microphone (model 46AP, GRAS Sound and Vibration, Holte, Denmark) is flush-mounted at the interface between the glass wool and the backing plate for recordings of the sound pressure at the interface (see Fig. 6). An OmniSource Loudspeaker type 4295 (Brüel & Kjær, Nærum, Denmark) is fixed on a rail that travels along a metallic beam. The metallic beam that contains the rail also translates vertically, allowing to place the source at variable angles of incidence. The measurements are performed with a scanning robot UR5 (Universal Robots, Odense, Denmark) programmed to move a 1/2 inch free-field microphone (model 46AC, GRAS Sound and Vibration, Holte, Denmark) in the vicinity of the sample. The microphone is fixed to a 1.22 m aluminum rod so as to reduce scattering induced by the robot from reaching the measurement aperture³⁹. Note that the use of sequential measurements with a robotic arm and a single microphone, in place of a traditional microphone array, makes it possible to circumvent positioning errors (positioning accuracy of approximately 1 mm given the rod length) and transducer mismatch errors³⁹, and to achieve a greater sampling capability than conventional microphone arrays. The robot creates an array of 162 microphone positions, arranged in two square layers of 9 × 9 positions each, with a vertical spacing of 3 cm between the two layers, a horizontal spacing of 2.5 cm, and an array aperture of 20 cm × 20 cm. The array is placed 1.5 cm away from the glass wool surface so as to guarantee a short back-propagation distance (and, as such, minimize reconstruction errors^{24,33,40}) while avoiding the influence of surface waves.

The source is driven with an exponential sine sweep ranging from 400 Hz to 5 kHz, with a duration of 2 s. Below 400 Hz, the measurement may be affected by diffraction phenomena resulting from the sample and backing

plate edges^{24,25}. The source is kept at a minimum distance of 1.5 m from the microphone array to guarantee approximate plane wave incidence on the measurement aperture at all frequencies (at 400 Hz, 1.5 m correspond to a source-array distance larger than a wavelength, ensuring that the sound pressure and particle velocity are approximately in phase; besides, 1.5 m corresponds to roughly 8 times the size of the measurement aperture, suggesting that the curvature of the wavefronts is negligible on the measurement grid). The frequency response is measured at the 162 positions with a frequency resolution of 0.5 Hz. The background noise is recorded every 20 microphone positions, resulting in a measured SNR around 46 dB in the frequency range 400 Hz to 5 kHz. The duration of a measurement sequence is approximately half an hour, including 8 s for the arm to stabilize after each displacement. The sequence runs automatically, based on the predefined positioning path.

Data availability

The datasets used and analyzed during this study are available from the corresponding author on reasonable request.

Code availability

The underlying code for this study is not publicly available but may be made available to qualified researchers on reasonable request from the corresponding author.

Received: 2 December 2024; Accepted: 27 May 2025;

Published online: 06 August 2025

References

1. Jaouen, L., Gourdon, E. & Glé, P. Estimation of all six parameters of Johnson-Champoux-Allard-Lafarge model for acoustical porous materials from impedance tube measurements. *J. Acoust. Soc. Am.* **148**, 1998–2005 (2020).
2. ISO 10534-2:1998. Determination of sound absorption coefficient and impedance in impedance tubes, part 2: Transfer-function method (1998). (International Organization for Standardization, Geneva, Switzerland).
3. Attenborough, K. Acoustical characteristics of porous materials. *Phys. Rep.* **82**, 179–227 (1982).
4. Song, B. H. & Bolton, J. S. A transfer-matrix approach for estimating the characteristic impedance and wave numbers of limp and rigid porous materials. *J. Acoust. Soc. Am.* **107**, 1131–1152 (2000).
5. Johnson, D. L., Koplik, J. & Dashen, R. Theory of dynamic permeability and tortuosity in fluid saturated porous media. *J. Fluid Mech.* **176**, 379–402 (1987).
6. Lafarge, D., Lemarinier, P., Allard, J.-F. & Tarnow, V. Dynamic compressibility of air in porous structures at audible frequencies. *J. Acoust. Soc. Am.* **102**, 1995–2006 (1997).
7. Attenborough, K. The prediction of oblique-incidence behaviour of fibrous absorbents. *J. Sound Vib.* **14**, 183–191 (1971).
8. Price, W. J. & Huntington, H. B. Acoustic properties of anisotropic materials. *J. Acoust. Soc. Am.* **22**, 32–37 (1950).
9. Allard, J.-F., Bourdier, R. & L'Esperance, A. Anisotropy effects in glass wool on normal impedance in oblique incidence. *J. Sound Vib.* **114**, 233–238 (1987).
10. Sanchez-Palencia, E. In *Non-homogeneous Media and Vibration Theory* (Springer-Verlag, Berlin, 1980).
11. Allard, J.-F. & Atalla, N. In *Sound Propagation in Porous Media: Modelling Sound Absorbing Materials, Second Edition* (John Wiley & Sons, Ltd, London, 2009).
12. Cavalieri, T. et al. Acoustic wave propagation in effective graded fully anisotropic fluid layers. *J. Acoust. Soc. Am.* **146**, 3400–3408 (2019).
13. Burke, S. The absorption of sound by anisotropic porous layers. *J. Acoust. Soc. Am.* **74**, S58 (1983).
14. Castagnede, B., Aknine, A., Melon, M. & Depollier, C. Ultrasonic characterization of the anisotropic behavior of air-saturated porous materials. *Ultrasonics* **36**, 323–341 (1998).
15. Tarnow, V. Measurements of anisotropic sound propagation in glass wool. *J. Acoust. Soc. Am.* **108**, 2243–2247 (2000).
16. Li, Z., Aydin, K. & Ozbay, E. Determination of the effective constitutive parameters of bi-anisotropic materials from reflection and transmission coefficients. *Phys. Rev. E* **79**, 026610 (2009).
17. Jiang, A. H., Bossard, J. A., Wang, X. & Werner, D. H. Synthesizing metamaterials with angularly independent effective medium properties based on an anisotropic parameter retrieval technique coupled with a genetic algorithm. *J. Appl. Phys.* **109**, 013515 (2011).
18. Castanié, A., Mercier, J.-F., Félix, S. & Maurel, A. Generalized method for retrieving effective parameters of anisotropic materials. *Opt. Express* **22**, 29937–29953 (2014).
19. Park, J. H., Lee, H. J. & Kim, Y. Y. Characterization of anisotropic acoustic metamaterial slabs. *J. Appl. Phys.* **119**, 034901 (2016).
20. Berzborn, M. & Vorländer, M. Inference of the acoustic properties of transversely isotropic porous materials. In *Proc. Internoise 2024* (Nantes, France, 2024).
21. Terroir, A. et al. General method to retrieve all effective acoustic properties of fully anisotropic fluid materials in three-dimensional space. *J. Appl. Phys.* **125**, 025114 (2019).
22. Morin, L. et al. Impedance tube measurements of the effective acoustic properties of anisotropic porous media. In *Proc. Forum Acusticum 2023*, 4619–4622 (Torino, Italy, 2023).
23. Cavalieri, T., Nolan, M., Gaborit, M. & Groby, J.-P. Experimental characterization of fully-anisotropic equivalent fluids from normal incidence measurements. *J. Sound Vib.* **608**, 119051 (2025).
24. Richard, A., Fernandez-Grande, E., Brunskog, J. & Jeong, C.-H. Estimation of surface impedance at oblique incidence based on sparse array processing. *J. Acoust. Soc. Am.* **141**, 4115–4125 (2017).
25. Richard, A. & Fernandez-Grande, E. Comparison of two microphone array geometries for surface impedance estimation (I). *J. Acoust. Soc. Am.* **146**, 501–504 (2019).
26. Nicolson, A. M. & Ross, G. F. Measurement of the intrinsic properties of materials by time-domain techniques. *IEEE Trans. Instrum. Meas.* **19**, 377–382 (1970).
27. Weir, W. B. Automatic measurement of complex dielectric constant and permeability at microwave frequencies. *Proc. IEEE* **62**, 33–36 (1974).
28. Pierce, A. D. In *Acoustics: An Introduction to Its Physical Principles and Applications* (Acoustical Society of America, New York, 1989), 2nd edn.
29. Auriault, C., Boutin, J.-L. & Geindreau, C. In *Homogenization of coupled phenomena in heterogeneous media* (ISTE Ltd and Wiley, London, 2009).
30. Bécot, F.-X. & Jaouen, L. Ceiling characterization and simulations (2010). (Report R201025, Matelys - Acoustique et Vibrations, Vaulx-en-Velin, France).
31. Biot, M. A. The theory of propagation of elastic waves in a fluid-saturated porous solid. I. Low frequency range. II. Higher frequency range. *J. Acoust. Soc. Am.* **28**, 168–191 (1956).
32. Williams, E. G. Regularization methods for near-field acoustical holography. *J. Acoust. Soc. Am.* **110**, 1976–1988 (2001).
33. Hald, J. Basic theory and properties of statistically optimized near-field acoustical holography. *J. Acoust. Soc. Am.* **125**, 2105–2120 (2009).
34. Nolan, M., Verburg, S. A., Brunskog, J. & Fernandez-Grande, E. Experimental characterization of the sound field in a reverberation room. *J. Acoust. Soc. Am.* **145**, 2237–2246 (2019).
35. Williams, E. In *Fourier Acoustics: Sound Radiation and Near-Field Acoustical Holography*, chap. 2 (Academic Press, New York, 1999).
36. Hansen, P. C. Discrete inverse problems: Insight and algorithms. In *Vol. 7 of Fundamentals of Algorithms* (SIAM, Philadelphia, PA, 2010).
37. Tikhonov, A. N. & Arsenin, V. I. A. Solutions of ill-posed problems. In *Scripta Series in Mathematics* (Winston, Silver Spring, MD, 1977).
38. Hansen, P. C. Analysis of discrete ill-posed problems by means of the l-curve. *SIAM Rev.* **34**, 561–580 (1992).
39. Verburg, S. A. & Fernandez-Grande, E. Reconstruction of the sound field in a room using compressive sensing. *J. Acoust. Soc. Am.* **143**, 3770–3779 (2018).

40. Fernandez-Grande, E., Jacobsen, F. & Leclere, Q. Sound field separation with sound pressure and particle velocity measurements. *J. Acoust. Soc. Am.* **132**, 3818–3825 (2012).

Acknowledgements

The authors would like to thank Henrik Hvidberg for help with the experimental arrangement, and Saint-Gobain Ecophon (Hyllinge, Sweden) for providing the glass wool samples. This work is funded by the Independent Research Fund Denmark, under DFF Individual International Post-doctoral Grant 1031-00012. The funder played no role in the study design, data collection, analysis, and interpretation of data, or the writing of this manuscript.

Author contributions

M.N. and J.-P.G. conceived the idea. M.N. developed the code and performed the simulations. M.N., S.A.V. and E.F.-G. conceived the experiment. M.N. and S.A.V. built the setup and performed all the measurements. T.C. performed the optimization. M.N. processed the data and wrote the manuscript. All authors participated in the analysis of results and discussions and reviewed the manuscript.

Competing interests

The authors declare no competing interests.

Additional information

Supplementary information The online version contains supplementary material available at <https://doi.org/10.1038/s44384-025-00016-7>.

Correspondence and requests for materials should be addressed to Mélanie Nolan.

Reprints and permissions information is available at <http://www.nature.com/reprints>

Publisher's note Springer Nature remains neutral with regard to jurisdictional claims in published maps and institutional affiliations.

Open Access This article is licensed under a Creative Commons Attribution-NonCommercial-NoDerivatives 4.0 International License, which permits any non-commercial use, sharing, distribution and reproduction in any medium or format, as long as you give appropriate credit to the original author(s) and the source, provide a link to the Creative Commons licence, and indicate if you modified the licensed material. You do not have permission under this licence to share adapted material derived from this article or parts of it. The images or other third party material in this article are included in the article's Creative Commons licence, unless indicated otherwise in a credit line to the material. If material is not included in the article's Creative Commons licence and your intended use is not permitted by statutory regulation or exceeds the permitted use, you will need to obtain permission directly from the copyright holder. To view a copy of this licence, visit <http://creativecommons.org/licenses/by-nc-nd/4.0/>.

© The Author(s) 2025